Developing Vicarious Calibration for Microwave Sounding Instruments Using Lunar Radiation

Hu Yang, *Member, IEEE*, Jun Zhou, *Member, IEEE*, Fuzhong Weng, Ninghai Sun, Kent Anderson, Quanhua Liu, and Edward J. Kim

***Abstract*— Accurate global observations from space are critical for global climate change study. However, atmospheric temperature trend derived from spaceborne microwave instruments remains a subject of debate, due mainly to the uncertainty in characterizing the long-term drift of instrument calibration. Thus, a highly stable target with a well-known microwave radiation is required to evaluate the long-term calibration stability. This paper develops a new model to simulate the lunar emission at microwave frequencies, and the model is then used for monitoring the stability of the Advanced Technology Microwave Sounder (ATMS) onboard Suomi NPP satellite. It is shown that the ATMS cold space view of lunar radiation agrees well with the model simulation during the past five years and this instrument is capable of serving the reference instrument for atmospheric temperature trending studies, and connecting the previous generation of microwave sounders from NOAA-15 to the future Joint Polar Satellite System Microwave Sounder onboard NOAA-20 satellite.**

***Index Terms*— Lunar calibration, microwave radiometer.**

I. Introduction

ACCURATE global observations from space are critical for global climate change study. However, atmospheric temperature trends derived from satellite instruments remain a subject of debate [1]–[4], due mainly to long-term drift and degradation, as well as calibration corrections made to instrument components. It is a common understanding in satellite calibration community that the assessment of long-term on-orbit satellite calibration stability is difficult, attribute to lack of stable reference targets. Currently, the widely used methods to assess the long-term instrument stability include vicarious calibration [5] and simultaneous nadir overpass cross calibration [6]. Recently, Draper *et al.* [7] and Brown *et al.* [8] use the noise diode to evaluate global precipitation measurement mission microwave imager calibration stability. Their methods can only provide the information of relative stability of the instruments since the diodes may become unstable. Therefore, to understand the long-term gain stability for climate research, the observations from a permanent reference target (PRT) with stable radiation property and well-known microwave brightness temperature are needed.

Lunar radiation is highly stable in microwave spectrum, attributing to the stable geophysical property of the moon's surface. The major factors that may change the magnitude of lunar microwave radiation in satellite instrument field of view (FOV) include the phase angle and position within FOV. Therefore, the moon surface radiation can be used as a PRT to evaluate the calibration accuracy and assess the long-term calibration stability for microwave radiometers. Indeed, the lunar observations can be obtained from most of the microwave sounders such as Advanced Microwave Sounding Unit and Advanced Technology Microwave Sounder (ATMS) when the antenna scans the cold space for calibration and the lunar radiation enters the antenna main lobe [9]. This so-called lunar intrusion (LI) can happen several times a year, and last two–three days each time. Therefore, many lunar observation samples are obtained during the instrument lifetime for us to calibrate and evaluate the long-term stability of the microwave sounding instruments.

SNPP is the first in the series of U.S. Joint Polar Satellite System (JPSS) and carries the ATMS instrument onboard. The overall on-orbit calibration accuracy of ATMS is better than 0.5 K, and the other performance parameters are well documented in many of our previous publications. In Section II, identification and calibration of lunar observation from SNPP ATMS are described. A general model is developed for simulating the lunar brightness temperatures in Section III. Section IV is lunar model validation and application in long-term calibration stability assessment. Summary and discussion are provided in Section V.

II. SNPP ATMS Lunar Observation Data Sets

For total power microwave sounding radiometers, its on-board calibration is achieved by periodically observing the cold space and an internal blackbody target. In particular for ATMS, it has two receiving antennas, with one receiving antenna serving for channels 1–15 with frequencies below

Manuscript received November 10, 2017; revised February 17, 2018 and April 19, 2018; accepted May 15, 2018. Date of publication June 26, 2018; date of current version October 25, 2018. This work was supported by NOAA (Cooperative Institute for Climate and Satellites) at the University of Maryland/ESSIC under Grant NA14NES4320003. *(Corresponding author: Hu Yang.)*

H. Yang and J. Zhou are with the Earth System Science Interdisciplinary Center, University of Maryland, College Park, MD 20742 USA (e-mail: huyang@umd.edu).

F. Weng, N. Sun, and Q. Liu are with the Center for Satellite Applications and Research, NOAA/NESDIS, College Park, MD 20740 USA.

K. Anderson is with Northrop Grumman Electronic Systems, Azusa, CA 91702 USA.

E. J. Kim is with the Goddard Space Flight Center, NASA, Greenbelt, MD USA.

Color versions of one or more of the figures in this paper are available online at http://ieeexplore.ieee.org.

Digital Object Identifier 10.1109/TGRS.2018.2841997

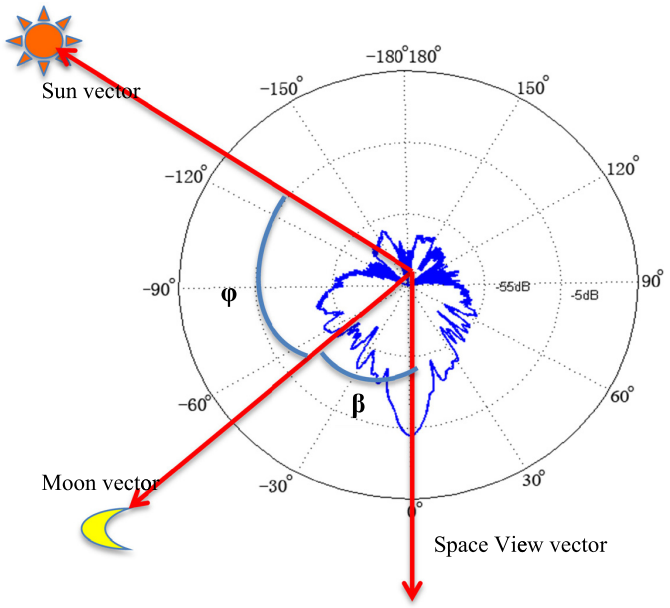

Fig. 1. Sketch plot of lunar observations from ATMS space view. The space view vector, moon vector, and sun vector are plotted in polar coordinate system of antenna pattern, with origin at the beam center.

60 GHz and a separate receiving antenna for channels 16–22 with frequencies above 60 GHz. There are four cold space view profiles located at 76.7°, 80°, 81.7°, and 83.4°, respectively, from the nadir. Which are referred as SP1, SP2, SP3, and SP4, with SP1 in satellite platform side and SP4 close to the earth side. For each profile, the cosmic background radiation is sampled four times consecutively with each sample spaced 1.11° apart, which are referred as SPV1, SPV2, SPV3, and SPV4. SPV1 is the closest to the earth, and SPV4 is the closest to the satellite platform. In the current ATMS operation, profile SP1 is selected to be used for calibration. More details about ATMS instrument characteristics and on-orbit calibration can be found from the recent studies by Yang and Weng [12]. As shown in Fig. 1, during the LI events, lunar observations can be obtained when the moon enters FOV of one of the four space view samples.

For ATMS like polar-orbiting microwave radiometers, there are six–seven LI events that can be captured through the whole year. Attribute to the moon's orbit characteristics, for NPP ATMS, the LI events most likely happened in January–June and November–December. The average duration time can be 2–3 days for each LI event. Therefore, there will be enough lunar measurement samples for instrument calibration as well as lifetime gain stability monitoring.

A. Lunar Observation Identification

For microwave sensors like ATMS, the magnitude of effective lunar radiation is closely related to the separation angle between the moon and space view β, apparent angle of moon α_l, beamwidth $\theta_{3\ \mathrm{dB}}$, and antenna solid angle at a specific channel. Therefore, space view observations with lunar appearing in its FOVs can be identified from the space view counts by the metric in the following [9]:

$$0 \le \beta' \le 1.25 \times \theta_{3\ \mathrm{dB}} \tag{1}$$

where $\beta' = |\beta + \alpha_l|$, α_l is calculated as

$$\alpha_l = \frac{r_{\mathrm{moon}}}{D_{\mathrm{moon}}}$$

where $r_{\mathrm{moon}} = 1737.92$ km and is the radius of the moon, and D_{moon} is the distance between satellite and the moon, which varies with satellite position in orbit. Since the receiver outputs at different space view positions are generally impacted by cosmic background radiation, lunar radiation, gain fluctuation, as well as random fluctuation of instrument to derive the clean lunar observations, the difference between maximum and minimum receiver output space view counts was used instead of using the original space view (SPV) count at a single scan position. Fig. 2(a) shows a typical case of the extracted lunar observations at ATMS channel 16 (with 2.2° beamwidth). The corresponding β angle is also presented in Fig. 2(b). It is shown that the variation of lunar radiation intensity (in count) varies with β. Moon displays its impacts when it begins entering the FOV, and reaches a maximum at the center of the FOV, then fading away when it moving out of FOV of space view. It should be noted that for the lunar observation data, we collected from SNPP ATMS, the lunar phase angle is around $110° \pm 5°$, only with a small variation [as shown in Fig. 2(c)].

B. Lunar Microwave Brightness Temperature Calibration

To derive the effective brightness temperature of the moon's disk, only those LI cases with at least one clean cold space view without lunar contamination were selected. Therefore, the effective brightness temperature of the moon's disk can be derived from calibration equation as follows:

$$\mathrm{TB}^{\mathrm{eff}}_{\mathrm{moon}} = \left[\frac{T_w - T_c}{C_w - C_c^{\mathrm{min}}}\right] \Delta C_{\mathrm{moon}} \tag{2}$$

where T_w and T_c are the warm load brightness temperature and cold space brightness temperature, C_w and C_c^{min} are warm load counts and the minimum cold counts within a scan, ΔC_{moon} is the difference between space view counts with maximum lunar radiation and the space view counts without lunar contamination at each scan. Note that to derive the reliable calibration results, T_w and T_c are further corrected for warm bias, earth sidelobe contamination correction, as well as the reflector emission contamination correction [12]. Fig. 3 shows a typical case of the extracted and calibrated lunar brightness temperature at ATMS channels 1, 16, and 22 (with 5.2°, 2.2°, and 1.1° beamwidth). It shows that the maximum effective lunar brightness temperature is about 1 K at K-/Ka-band, increase to 8 K at W-band, and can reach as large as more than 20 K at G-band.

III. Lunar Microwave Brightness Temperature Model

The major challenge is how to accurately calculate the effective brightness temperature of the moon when it appears in the FOV of microwave instruments. Currently, there is no effective lunar brightness temperature model available for microwave sensors. For most of the current spaceborne microwave instruments, the moon only fills a fraction of the

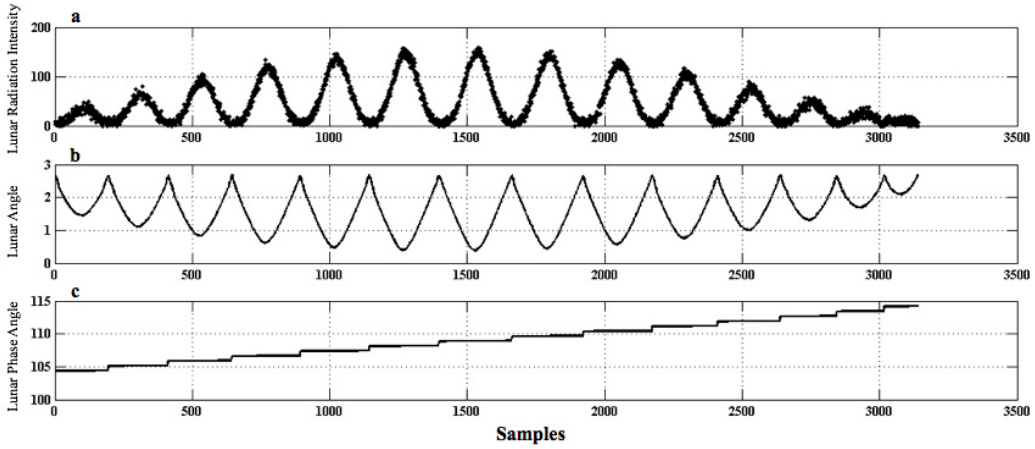

Fig. 2. Typical case of the extracted lunar observations at ATMS channel 16. (a) Lunar radiation intensity in counts. (b) Lunar observations angle in degree. (c) Lunar phase angle in degree.

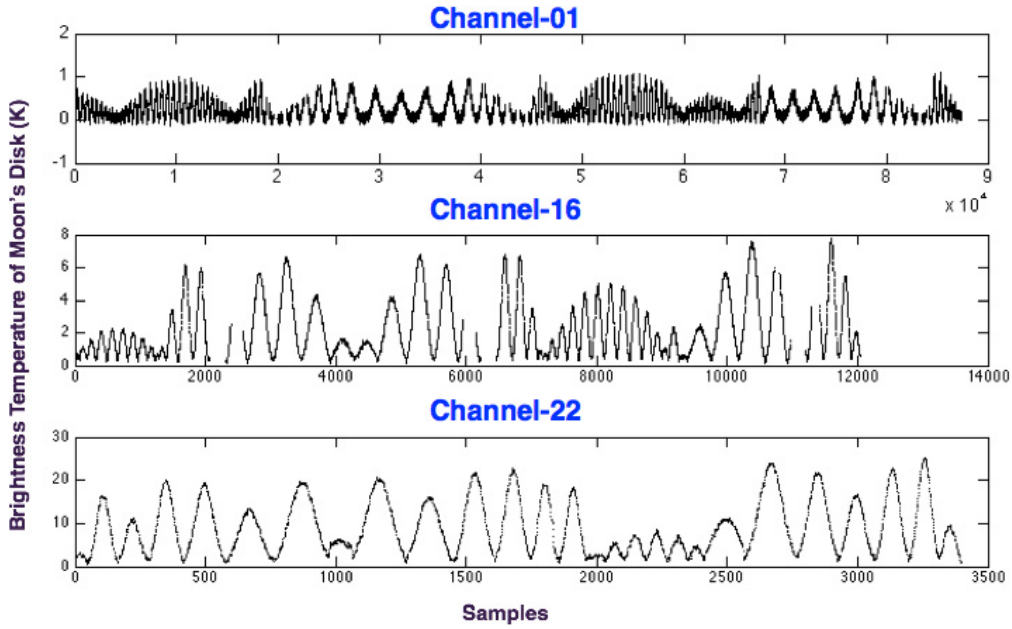

Fig. 3. Typical case of the calibrated lunar brightness temperature at ATMS channels 1, 16, and 22 (with 5.2°, 2.2°, and 1.1° beamwidth).

FOV. The impact of the antenna pattern is important and needs to be considered when calculating the effective brightness temperature of the moon's disk. In addition, a physical model is also required to calculate the average brightness temperature of the moon's disk in microwave spectrum region. Furthermore, the antenna beam pointing accuracy should be known. In Sections III-A–III-C, we will demonstrate that by combined satellite observations and ground-measured antenna pattern data sets, a physical model for calculating the effective microwave brightness temperature of the moon's disk can be established for use in microwave calibration.

A. Thermal Emission Properties of the Moon's Surface

Research has been extensively carried out to study the thermal emission from the moon in past years [13]–[19]. The observations from the Diviner Lunar Radiometer Experiment (DLRE) instrument onboard the Lunar Reconnaissance Orbiter revealed a strong diurnal variation of lunar surface temperature ranging from 95 to 397 K [20]. By using the DLRE observations from 2009 to 2015, the surface temperature averaged within 1° spatial resolution with moon phase angle, φ ranging from $-180°$ to 180° can be derived and is shown in Fig. 4(a). Lunar surface temperature varies with latitude and phase angle, and reaches the maximum at $\varphi = 0$ and the minimum at $\varphi = 180$. At each phase angle, the temperatures decrease with latitude with the highest at the moon's equator. For ATMS, since the apparent angle of lunar is smaller than its antenna beamwidth, only the average temperature of the moon's disk is interested, which can be derived by averaging over the global temperature at each phase angle by using the DLRE temperature data sets mentioned above. As shown in Fig. 4(b), the dynamic range of physical

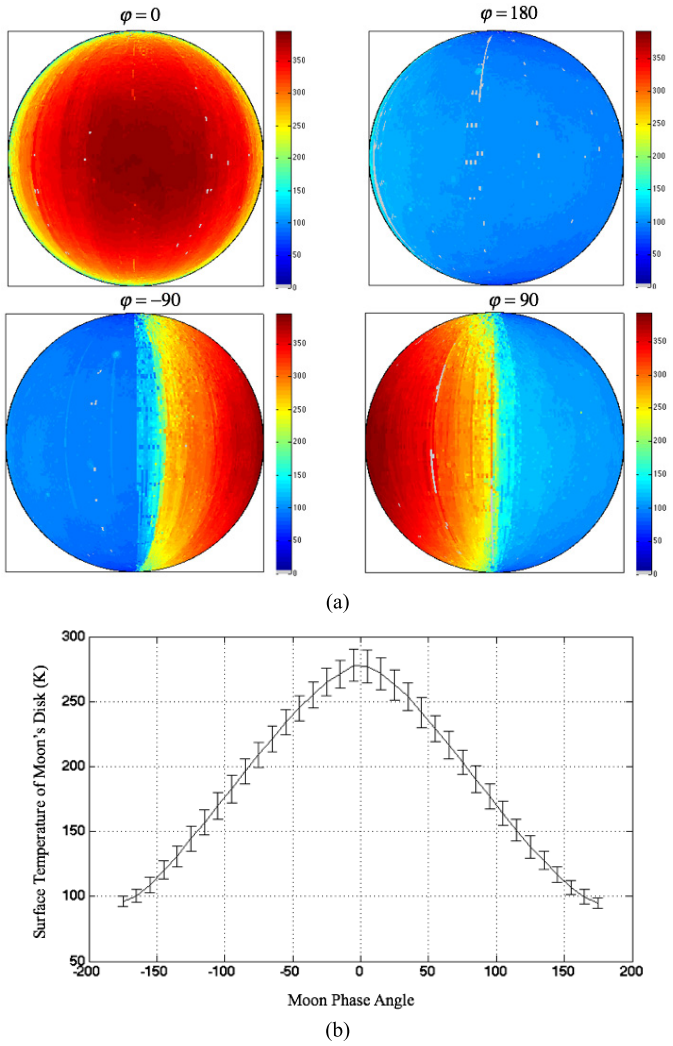

Fig. 4. (a) $1^\circ \times 1^\circ$ resolution global mean moon surface temperature generated from DLRE observations. For each pixel in the map of different moon phase angles, surface temperature was averaged over the observations from 2009 to 2015. (b) Mean and standard deviation of surface temperature of the moon's disk derived from DLRT data sets.

temperature of the moon's disk changes from 94 to 270 K, with a standard deviation from 4 to 10 K. The average physical temperature of the moon's disk can be well modeled as a function of moon phase angle φ by using a regression model as follows:

$$T_{\text{moon}} = 100.89 + 85.65(1 - \cos\varphi) - 0.24(1 + \cos 2\varphi). \quad (3)$$

Microwave radiation can penetrate to lunar subsurface; thus, the microwave thermal emission in terms of brightness temperature can be quite different from skin temperature. Previous studies show that due to the special structure of the moon's surface and the penetration characteristic of microwave radiation, the maximum microwave emission from the moon typically lags behind the maximum temperature at the full moon. The lag angle depends on the ratio of the emission layer physical thickness to the penetration depth [21]. Based on the ground microwave radiometer observations operating at 1.25-cm wavelength (24 GHz), Piddington and Minnett [22] observed a 45° phase lag of microwave brightness temperature behind the moon's surface temperature. Recent observations from Chinese Chang-e moon orbit microwave radiometer MRM show 30° phase lag in 37-GHz brightness temperature [23]. The overall goal of this paper is to establish a general lunar calibration model for all microwave sounders, but due to lack of data samples of microwave lunar observations being collected under different lunar phase angles, currently there is no phase lag term included in our model. Note that for lunar observations from polar-orbit microwave radiometers, the lunar phase angle is pretty stable and only has limited dynamic range of around $110^\circ \pm 5^\circ$; therefore, lack of phase angle term will not affect the model accuracy. The phase lag term will be studied when lunar observations in different lunar phases can be collected from future small/cubic satellite microwave instruments.

Observations and experiments after the Apollo missions have disclosed that lunar surface consists of a series of layers of material ejected from individual meteorite craters over a period of time, and embedded lava flows and pyroclastic deposits. Apollo 15 and 17 heat flow experiments disclosed that there is a big drop in temperature about 100 K within the upper lunar regolith of a few centimeters (2 cm) [24], [25]. Now it is widely accepted that lunar subsurface composition is composed of three homogeneous media: regolith with depth extend from several meters to tens of meters, rock and ice,

TABLE I
SNPP ATMS ANTENNA POINTING ERROR EULER ANGLES

Chan	Roll	Pitch	Yaw
1	-0.034	0.229	-0.031
2	0.161	0.328	0.052
3	-0.207	0.128	-0.159
4	-0.207	0.128	-0.167
5	-0.207	0.128	-0.169
6	-0.207	0.128	-0.168
7	-0.207	0.128	-0.168
8	-0.207	0.128	-0.164
9	-0.207	0.128	-0.173
10	-0.207	0.128	-0.167
11	-0.207	0.128	-0.165
12	-0.207	0.128	-0.167
13	-0.207	0.128	-0.167
14	-0.207	0.128	-0.168
15	-0.207	0.128	-0.167
16	-0.069	-0.107	-0.008
17	0	0	-0.054
18	0	0	-0.052
19	0	0	-0.054
20	0	0	-0.052
21	0	0	-0.054
22	0	0	-0.055

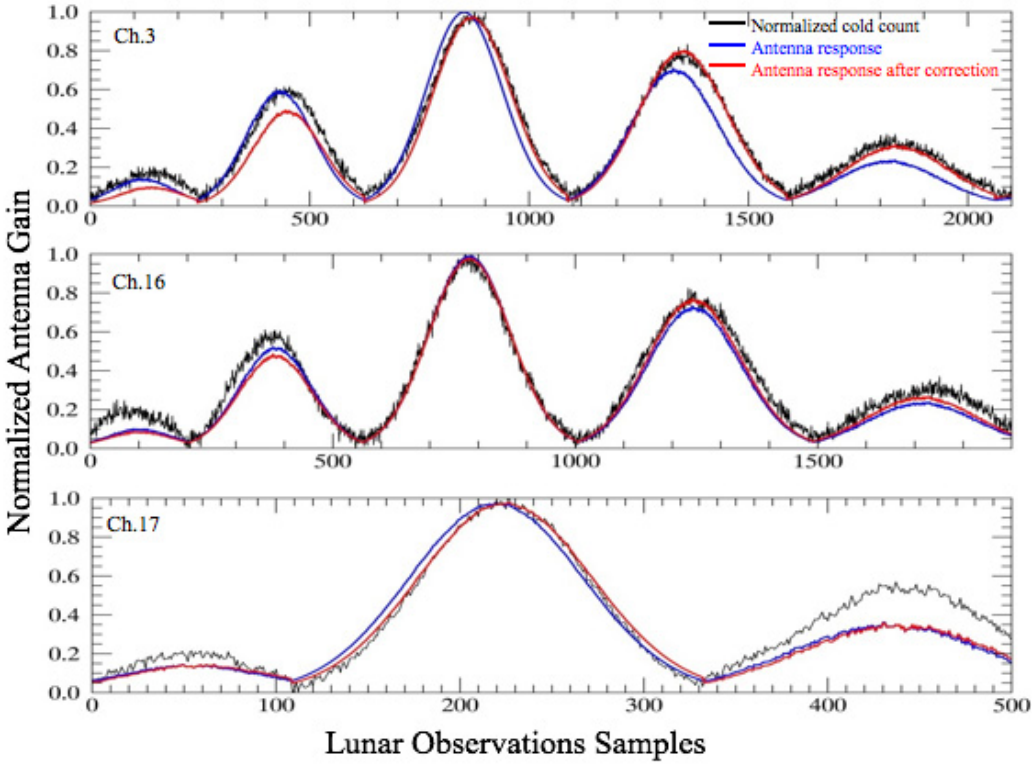

Fig. 5. Simulated antenna response with original antenna beam pointing angle (blue curve) and corrected pointing angles (red curve) at channels 3, 16, and 17 during lunar observation on January 6, 2017–January 8, 2017. Comparing with antenna pointing truth (normalized lunar observation counts in black line), the pointing error in antenna response function has been largely reduced.

placed in different orders at different depths beneath the surface. In [24]–[28], an incoherent model was adopted for lunar microwave emission simulation, in which the volume scattering contribution is negligible with respect to that due to absorption. According to Montopoli's study [24], [25], at equatorial region, the moon's surface temperature varies dramatically at near surface from 100 to 350 K, and then becomes stable with depth increasing to more than 5 m. Montopoli *et al.* [25] found that at 24-GHz microwave waveband, no stratigraphy change is sensed for depths larger than about 0.15 m. Based on the previous studies mentioned above, due to lack of vertical temperature profile information of regolith and the difficulty to establish an accurate multilayer microwave emissivity model for lunar surface, the approach to calculate emissivity from a theoretical model will not be adopted in this paper. Instead, we will derive the effective surface emissivity spectrum of the moon's disk $E_{\text{moon}}^{\text{disk}}$ from physical temperature T_{moon} and well-calibrated brightness temperature $\text{TB}_{\text{moon}}^{\text{disk}}$ by using the following equation:

$$\text{TB}_{\text{moon}}^{\text{disk}} = E_{\text{moon}}^{\text{disk}} \times T_{\text{moon}}. \tag{4}$$

In (3), brightness temperature $\text{TB}_{\text{moon}}^{\text{disk}}$ and physical temperature T_{moon} of the moon's disk can be calculated from (2) and (3), respectively. Considering the fact that for a certain lunar phase, the emissive property of the moon's surface in microwave spectrum is extremely stable, the emissivity spectrum determined from the well-calibrated SNPP ATMS lunar observation samples can, therefore, be used in (4) to predict the average microwave brightness temperature of the moon's disk.

B. Antenna Pointing Error Correction

As pointed by Buehler *et al.* [29], beam pointing error can have significant impact on accuracy of lunar model simulation, especially when the moon appears in center of FOV. The pointing error issue needs to be addressed before we can proceed to establish a reliable lunar radiation model. Studies shows that the static error originates from the beam misalignment and the instrument mounting error is the dominant part in the SNPP ATMS antenna pointing error [30]. Even though these static error terms have been measured in the prelaunch ground test and corrected in geolocation process, residual errors may still exist due to the on-orbit thermal dynamic change and shift during the launch. In this paper, based on [30], the beam pointing error was derived in terms of Euler angles from an algorithm combined using coastline inflection point and the drift curve of lunar observations, as listed in Table I, from which a correction matrix then can be constructed and applied in geolocation process to correct the beam pointing error in lunar observations. Fig. 5 shows the results of antenna beam pointing correction. It can be seen that the beam pointing error in the data has been largely reduced after the correction being applied.

C. Effective Lunar Microwave Brightness Temperature Model

For most of the current polar-orbit spaceborne microwave radiometers operating at around 800-km altitude earth orbit,

TABLE II
LUNAR MODEL PARAMETERS FOR NPP ATMS

Chan.	Ω_A	σ	E_{moon}^{disk}
1	36.002	2.3675	0.9040
2	36.002	2.3409	0.9083
3	5.866	0.9449	0.9557
4	5.866	0.9555	0.9529
5	5.866	0.9449	0.9573
6	5.866	0.9343	0.9585
7	5.866	0.9449	0.9598
8	5.866	0.9130	0.9664
9	5.866	0.9130	0.9670
10	5.452	0.8865	0.9551
11	5.452	0.8865	0.9588
12	5.452	0.8865	0.9614
13	5.452	0.8865	0.9598
14	5.452	0.8865	0.9558
15	5.452	0.8865	0.9649
16	5.425	0.8918	0.9738
17	1.754	0.4618	0.9221
18	1.754	0.4671	0.9458
19	1.754	0.4671	0.9452
20	1.754	0.4512	0.9463
21	1.754	0.4512	0.9433
22	1.754	0.4512	0.9442

the apparent angle of the moon's disk is about 0.5°, which is much smaller than beamwidth of ATMS observations. When the moon appears in satellite observation FOV, the effective microwave brightness temperature of the moon's disk, $\mathrm{TB}_{\mathrm{moon}}^{\mathrm{ref}}$, can be expressed as a function of the antenna response function G_{ant}, normalized solid angle of the moon Ω_{moon}, and average brightness temperature of the moon's disk as follows:

$$\mathrm{TB}_{\mathrm{moon}}^{\mathrm{ref}} = \Omega_{\mathrm{moon}} \times G_{\mathrm{ant}} \times \mathrm{TB}_{\mathrm{moon}}^{\mathrm{disk}}. \tag{5}$$

Assuming the azimuthal asymmetry is insignificant, the antenna response within the mean beam range can then be accurately simulated by 1-D Gaussian function

$$G_{\mathrm{ant}}(\beta) = e^{-\beta^2/2\cdot\sigma^2} \tag{6}$$

where β is the separation angle between antenna boresight and moon-in-view vector, and σ is the antenna parameter and defined as a function of 3-dB beamwidth $\theta_{3\ \mathrm{dB}}$

$$\sigma = (0.5 \times \theta_{3\ \mathrm{dB}})/\sqrt{2\log 2}.$$

The normalized solid angle of the moon is calculated as a solid angle of the moon disk normalized by the antenna beam solid angle, Ω_A

$$\Omega_{\mathrm{moon}} = \frac{\pi \left(\frac{r_{\mathrm{moon}}}{D_{\mathrm{moon}}}\right)^2}{\Omega_A} \tag{7}$$

where Ω_A is a beam solid angle, $\Omega_A = \int\int_{4\pi} G(\theta,\phi)\sin\theta d\theta d\theta d\varphi$. In this paper, antenna-related parameters σ and Ω_A were calculated from ground measurements of antenna pattern delivered by Vendor. To determine the effective microwave emissivity spectrum of lunar disk for ATMS channels, a total of 16 594 lunar observation samples from 14 LI events were collected

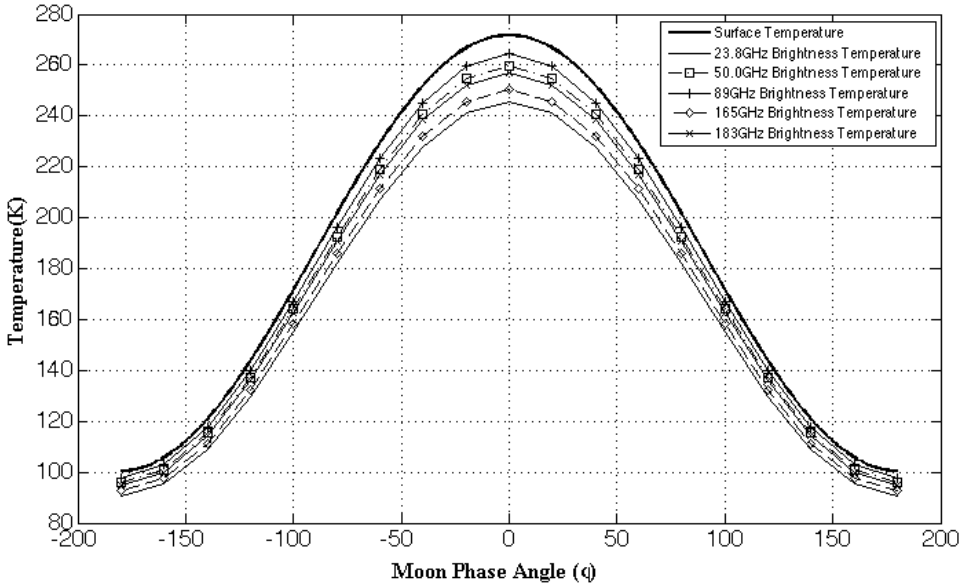

Fig. 6. Surface temperature and model simulated average microwave brightness temperature of the moon's disk at different frequencies and different moon phase angles.

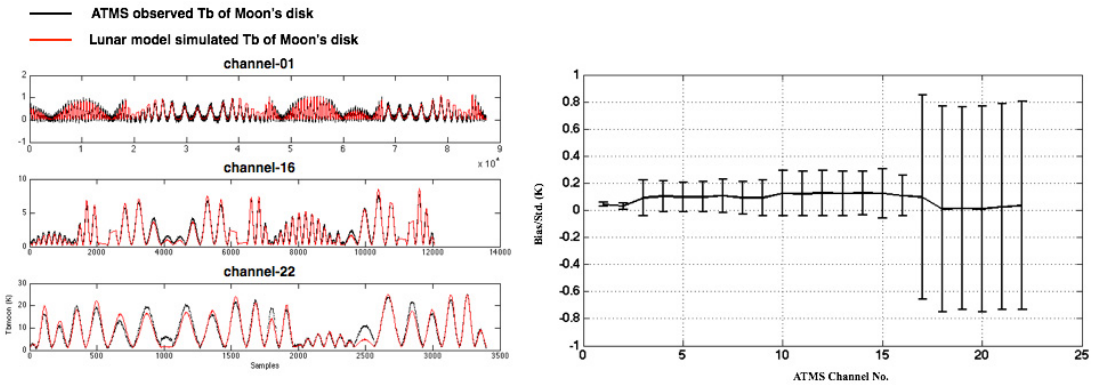

Fig. 7. (Left) Special case of lunar model validation and (Right) mean bias and standard deviation of lunar model for each channel of ATMS.

in 2013. The effective lunar disk brightness temperature were then calculated from (2) following a calibration process. Substituting (4) into (5) yields the lunar surface emissivity $E_{\text{moon}}^{\text{disk}}$, and a best fitting algorithm is applied for 22 channels of ATMS with frequency from 23.8 to 183 GHz. A frequency-dependent emissivity spectrum of lunar disk for ATMS channels can then be derived and listed in Table II, together with parameters σ and Ω_A. The retrieved average emissivity of the moon's disk has a minimum of 0.90 at K/Ka band (23/31 GHz) and a maximum of 0.97 at W-band (89 GHz). It should be noted that since there is about 10% uncertainty in G-band antenna pattern measurements for SNPP ATMS, a relatively larger bias is expected in lunar model for these channels. Fig. 6 shows the simulated average microwave brightness temperature of the moon's disk using (4) with phase angle ranging from new moon (180°) and full moon (0°), for frequencies from 24 to 183 GHz. It can be seen that the microwave brightness temperature shows frequency-dependent feature: the lower frequency of 23.8-GHz channel has a temperature variation from 90 to 245 K, which is smaller comparing to 98–265 K at 89-GHz channel. This conclusion is consistent with study results from [25] and can be explained by penetration depth of microwave observations and internal lunar heat flow. The decrease of brightness temperature in 165 and 183 GHz may due to the noise in antenna pattern measurements in high-frequency channels, which will lead to inaccurate calculation results of beam solid angle and therefore increase the error of retrieved emissivity in these channels.

IV. Lunar Model Validation and Application in Long-Term Calibration Stability Monitoring for SNPP ATMS Instrument

A. Lunar Model Validation Results

Lunar observations from ATMS instrument from January 2012 to January 2017 are collected and calibrated using (2), except for the observations in 2013. The calibrated effective lunar brightness temperature is then compared with the model simulations derived from (5). A special case of the validation is presented in Fig. 7, together with the mean bias and standard deviation from all data statistics for each

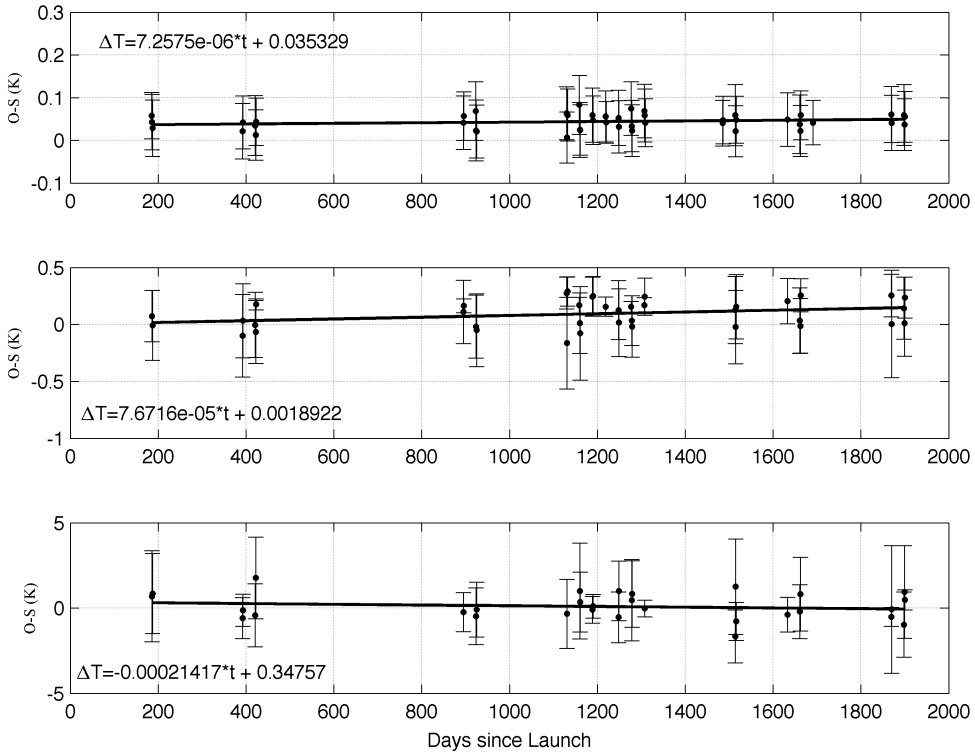

Fig. 8. SNPP ATMS calibration stability. Black points are variation of daily average ΔT_{moon}, solid lines are fitting trend. (From top to bottom) Channels 1, 8, and 17. Error margin was also presented as bar in gray.

channel. It is shown that while the mean bias is less than 0.1 K with a standard deviation around 0.2 K in K-, Ka-, W-, and V-bands, the standard deviation of model bias in G-band is conspicuously different with other channels and close to 1 K. This might be explained by the much higher noise of antenna pattern measurements in these high-frequency channels and, therefore, the larger error in lunar model as a result. Besides, the uncertainty in lunar surface temperature can also raise 1-K error in lunar model simulations for G-bands in worst cases. This might be the other major error source for model simulations in channels with small FOV size.

B. Long-Term Calibration Stability Monitoring for SNPP ATMS Instrument

As previously stated, lunar as a PRT can also help to evaluate the long-term calibration stability of microwave sensors. Here, the lunar brightness temperature model developed in this paper is used to simulate the effective brightness temperature of the moon's disk, and then compared with the measurements from ATMS instrument. Sensor calibration stability can then be evaluated as

$$S = d(\Delta T_{\text{moon}})/dt \tag{8}$$

where ΔT_{moon} is the difference between observed effective lunar brightness temperature $T_{\text{moon}}^{\text{eff}}$ defined in (2) and the simulated reference lunar brightness temperature $T_{\text{moon}}^{\text{ref}}$ calculated from lunar model defined in (5)

$$\Delta T_{\text{moon}} = T_{\text{moon}}^{\text{eff}} - T_{\text{moon}}^{\text{ref}}. \tag{9}$$

Fig. 8 shows the instrument long-term calibration stability evaluation results for ATMS observations from December 3, 2011 to January 13, 2017. Panels from top to bottom are variation of daily average ΔT_{moon} for channels 1, 8, and 20. The linear fitting line of ΔT_{moon} trend from six years of data is also presented. It is shown that for ATMS, the observed lunar T_b is highly consistent with the reference lunar T_b, with a mean bias of less than 0.5 K in general and 0.05 K for K-/Ka- and V-/W-bands in specific. SNPP ATMS shows a highly stable calibration status after 6-year on-orbit operation. The drift magnitude is less than 10^{-5} K/day for most of the channels.

V. Conclusion

Long-term instrument calibration stability assessment is very important for satellite data application in climate change study. In this paper, we developed a new method to evaluate instrument stability by taking the moon as a reference target. A parameterized physical model was established to simulate the lunar microwave brightness temperature from its phase and observation angle measurements. The model simulations can be taken as a reference to compare with observed lunar brightness temperatures to check the accuracy and stability of the instrument observations. The method is successfully applied to 5 years of lunar observations from Suomi NPP ATMS instrument. The model established in this paper can also be expanded to other microwave sounding instruments to assess their long-term calibration drift trend.

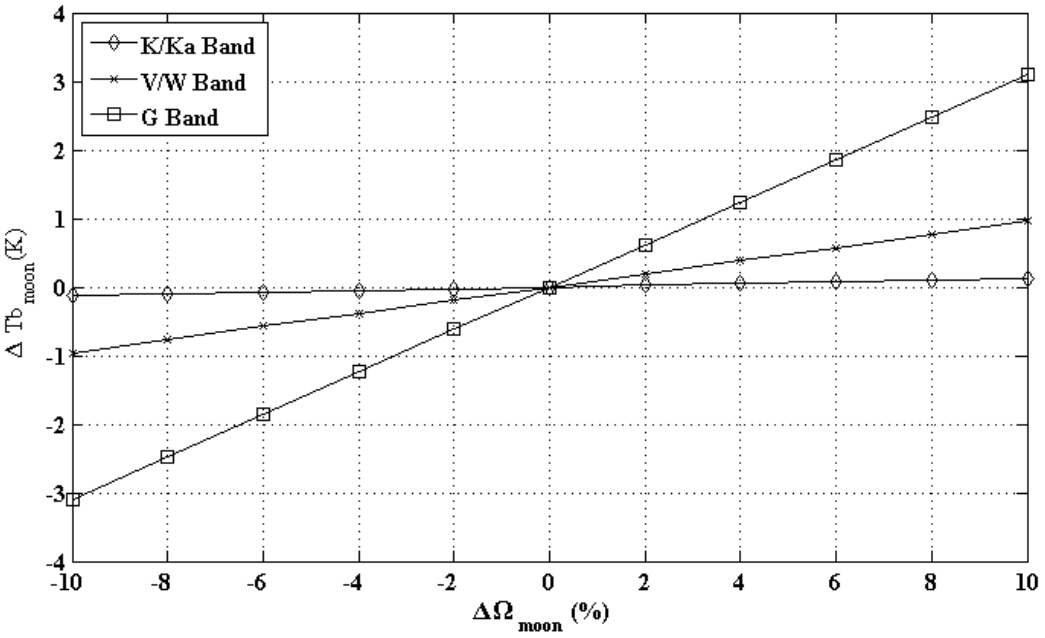

Fig. 9. Sensitivity of lunar model bias to antenna beam solid angle. x-axis is beam solid angle error in percentage, and y-axis is the corresponding model bias at channels with different FOV sizes.

Due to lack of satellite lunar observations in different lunar phases, we assume that the phase of microwave brightness temperature variation is kept the same with the surface temperature. But as some researchers pointed out that due to the special structure of the moon's surface and the penetration characteristic of microwave radiation, there might be a phase lag of microwave brightness temperature behind the moon's surface temperature. Phase angle in the model may further be adjusted when more lunar observations taken at different lunar phases are available in future.

It also needs to be noted that the accuracy of effective lunar radiation magnitude from microwave sensors is largely determined by the lunar solid angle. To investigate the impact of antenna beam angle to accuracy of lunar brightness temperature simulation model in (5), a sensitivity test was performed at full moon condition (moon phase angle is 180°). As shown in Fig. 9, sensitivity of lunar simulation model to antenna beam solid angle is beamwidth dependent: a 10% uncertainty of beam solid angle in lower frequency channel with FOV size of 5.2° can only raise a 0.13-K model simulation bias, while it will introduce as large as 3-K biases in channels with 1.1° beamwidth. From antenna pattern ground measurements for SNPP and JPSS-01 ATMS, we learned that the uncertainty in antenna beam solid angle in ATMS G-band is larger than 10%. This might explain the lunar model error in G-band found in Section IV. Therefore, accurate information of antenna beam solid angle is very important for successful implementation of the lunar model developed in this paper.

As demonstrated in this paper, a reliable lunar T_b model can be established from well-calibrated ATMS lunar observations, combined with accurate ground measurements of antenna pattern. Therefore, in future, it is possible to obtain the warm load equivalent effective lunar brightness temperature for calibration by using a finer beamwidth in lunar observations. This is especially important for on-orbit calibration of small and cubic satellites.

ACKNOWLEDGMENT

The authors would like to thank Prof. J.-P. Wiliams and Prof. D. A. Paige from the University of California, Los Angeles, CA, USA, for providing advice and help on Diviner Lunar Radiometer Experiment data sets. They would also like to thank Dr. V. R. Leslie from MIT/LL, Lexington, MA, USA, for his discussions and advices that are very helpful to not only this study, but also for future work on this topic.

REFERENCES

[1] J. R. Christy, R. W. Spencer, W. B. Norris, W. D. Braswell, and D. E. Parker, "Error estimates of version 5.0 of MSU–AMSU bulk atmospheric temperatures," *J. Atmospheric Ocean. Technol.*, vol. 20, no. 5, pp. 613–629, 2003.

[2] C. A. Mears and F. J. Wentz, "Construction of the remote sensing systems v3.2 atmospheric temperature records from the MSU and AMSU microwave sounders," *J. Atmos. Ocean. Technol.*, vol. 26, no. 6, pp. 1040–1056, 2009.

[3] K. Y. Vinnikov, N. C. Grody, A. Robock, R. J. Stouffer, J. D. Philip, and M. D. Goldberg, "Temperature trends at the surface and in the troposphere," *J. Geophys. Res., Atmospheres*, vol. 111, no. D3, p. D03106, 2006.

[4] F. Weng, X. Zou, and Z. Qin, "Uncertainty of AMSU-A derived temperature trends in relationship with clouds and precipitation over ocean," *Climate Dyn.*, vol. 43, nos. 5–6, pp. 1439–1448, 2014.

[5] C. S. Ruf, "Detection of calibration drifts in spaceborne microwave radiometers using a vicarious cold reference," *IEEE Trans. Geosci. Remote Sens.*, vol. 38, no. 1, pp. 44–52, Jan. 2000.

[6] C. Cao, F. Weng, M. Goldberg, X. Wu, H. Xu, and P. Ciren, "Inter-satellite calibration of polar-orbiting radiometers using the SNO/SCO method," in *Proc. IEEE Int. Geosci. Remote Sens. Symp. (IGARSS)*, Jul. 2005, p. 4.

[7] D. W. Draper, D. A. Newell, D. S. McKague, and J. R. Piepmeier, "Assessing calibration stability using the global precipitation measurement (GPM) microwave imager (GMI) noise diodes," *IEEE J. Sel. Topics Appl. Earth Observat. Remote Sens.*, vol. 8, no. 9, pp. 4239–4247, Sep. 2015.

[8] S. T. Brown, S. Desai, W. Lu, and A. B. Tanner, "On the long-term stability of microwave radiometers using noise diodes for calibration," *IEEE Trans. Geosci. Remote Sens.*, vol. 45, no. 7, pp. 1908–1920, May 2007.
[9] H. Yang and F. Weng, "Corrections for on-orbit ATMS lunar contamination," *IEEE Trans. Geosci. Remote Sens.*, vol. 54, no. 4, pp. 1918–1924, Apr. 2016.
[10] F. Weng and H. Yang, "Validation of ATMS calibration accuracy using Suomi NPP pitch maneuver observations," *Remote Sens.*, vol. 8, no. 4, p. 332, 2016.
[11] F. Weng *et al.*, "Calibration of Suomi National Polar-Orbiting Partnership advanced technology microwave sounder," *J. Geophys. Res., Atmospheres*, vol. 118, no. 19, pp. 11187–11200, 2013.
[12] H. Yang, F. Weng, and K. Anderson, "Estimation of ATMS antenna emission from cold space observations," *IEEE Trans. Geosci. Remote Sens.*, vol. 54, no. 8, pp. 4479–4487, Aug. 2016.
[13] Z. Wang, Y. Li, J. Jiang, and D. Li, "Lunar surface dielectric constant, regolith thickness, and ^{3}He abundance distributions retrieved from the microwave brightness temperatures of CE-1 Lunar Microwave Sounder," *Sci. China Earth Sci.*, vol. 53, no. 9, pp. 1365–1378, 2010.
[14] G. R. Olhoeft and D. W. Strangway, "Dielectric properties of the first 100 meters of the Moon," *Earth Planetary Sci. Lett.*, vol. 24, no. 3, pp. 394–404, 1975.
[15] R. C. Anderson, M. Buehler, S. Seshadri, G. Kuhlman, and M. Schaap, "Dielectric constant measurements for characterizing lunar soils," *Lunar Planetary Sci.*, vol. 36, pp. 1–14, Jan. 2005.
[16] V. Y. Ryadov, N. I. Furashov, and G. A. Sharonov, "Measurements of the Moon natural infrared thermal radiation," *Sov. Astron.*, vol. 8, p. 82, Jul./Aug. 1964.
[17] B. J. Sandor and R. T. Clancy, "Microwave observations and modeling of a lunar eclipse," *ICARUS*, vol. 115, no. 2, pp. 387–398, 1995.
[18] G.-P. Hu, Y.-C. Zheng, A.-A. Xu, and Z.-S. Tang, "Microwave brightness temperature of the Moon: The possibility of setting a calibration source of the lunar surface," *IEEE Trans. Geosci. Remote Sens.*, vol. 13, no. 2, pp. 182–186, Feb. 2016.
[19] W. Ji, L. Dihui, Z. Xiaohui, J. Jingshan, A. T. Altyntsev, and B. I. Lubyshev, "Microwave brightness temperature imaging and dielectric properties of lunar soil," *J. Earth Syst. Sci.*, vol. 114, no. 6, pp. 627–632, 2016.
[20] J.-P. Williams, D. A. Paige, B. T. Greenhagen, and E. Sefton-Nash, "The global surface temperatures of the Moon as measured by the Diviner Lunar Radiometer Experiment," *Icarus*, vol. 283, pp. 300–325, Feb. 2017.
[21] V. D. Krotikov and V. S. Troitskiĭ, "Radio emission and nature of the Moon," *Sov. Phys. Uspekhi*, vol. 6, no. 6, pp. 841–871, 1964.
[22] J. H. Piddington and H. C. Minnett, "Microwave thermal radiation from the Moon," *Austral. J. Sci. Res.*, vol. 2, no. 1, pp. 63–77, 1949.
[23] Y. C. Zheng, K. T. Tsang, K. L. Chan, Y. L. Zou, F. Zhang, and Z. Y. Ouyang, "First microwave map of the Moon with chang'E-1 data: The role of local time in global imaging," *Icarus*, vol. 219, no. 1, pp. 194–210, 2012.
[24] M. Montopoli, A. Di Carlofelice, M. Cicchinelli, P. Tognolatti, and F. S. Marzano, "Lunar microwave brightness temperature: Model interpretation and inversion of spaceborne multifrequency observations by a neural network approach," *IEEE Trans. Geosci. Remote Sens.*, vol. 49, no. 9, pp. 3350–3358, Sep. 2011.
[25] M. Montopoli, A. D. Carlofelice, P. Tognolatti, and F. S. Marzano, "Remote sensing of the Moon's subsurface with multifrequency microwave radiometers: A numerical study," *Radio Sci.*, vol. 46, no. 1, pp. 1–13, 2011.
[26] S. J. Keihm and J. A. Cutts, "Vertical-structure effects on planetary microwave brightness temperature measurements: Applications to the lunar regolith," *Icarus*, vol. 48, no. 2, pp. 201–229, 1981.
[27] S. J. Keihm, "Effects of subsurface volume scattering on the lunar microwave brightness temperature spectrum," *Icarus*, vol. 52, no. 3, pp. 570–584, 1982.
[28] S. J. Keihm, "Interpretation of the lunar microwave brightness temperature spectrum: Feasibility of orbital heat flow mapping," *ICARUS*, vol. 60, no. 3, pp. 568–589, 1984.
[29] S. A. Buehler, "The Moon as a photometric calibration standard for microwave sensors," *Atmospheric Meas. Techn.*, vol. 9, no. 8, pp. 3467–3475, 2016.
[30] J. Zhou, H. Yang, and F. Weng, "Validate and improve ATMS geolocation accuracy by using lunar observations," in *Proc. IEEE Int. Geosci. Remote Sens. Symp.*, Jul. 2017, pp. 244–247.

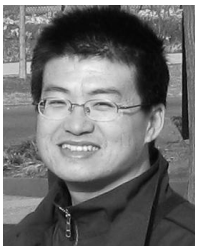

Hu Yang (M'09) received the Ph.D. degree from the Institute of Remote Sensing Application, Chinese Academy of Sciences, Beijing, China, in 2003.

From 2003 to 2011, he was a Senior Research Scientist with the National Satellite Meteorological Center, China Meteorological Administration, Beijing, leading the microwave instrument calibration and satellite ground application system development as an Instrument Scientist and a Program Scientist. In 2012, he joined the Earth System Science Interdisciplinary Center, University of Maryland, College Park, MD, USA, where he is currently a Project PI of the NPP/Joint Polar Satellite System Advanced Technology Microwave Sounder calibration/validation. He has authored over 40 peer-reviewed journals. His research interests include passive microwave radiometer calibration/validation, satellite geolocation, and satellite observation simulation.

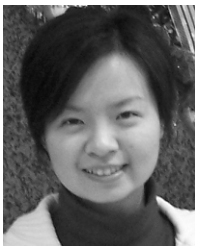

Jun Zhou (M'18) received the Ph.D. degree from the Institute of Atmospheric Physics, Chinese Academy of Sciences, Beijing, China, in 2010.

In 2015, she joined the Earth System Science Interdisciplinary Center, University of Maryland, College Park, MD, USA, where she is involved in the NPP/Joint Polar Satellite System Advanced Technology Microwave Sounder geolocation and validation. Her research interests include cloud tomography with microwave radiometer observations, satellite data assimilation, and satellite geolocation and validation.

Fuzhong Weng received the Ph.D. degree from the Department of Atmospheric Science, Colorado State University, Fort Collins, CO, USA, in 1992.

He is currently the Chief for satellite applications and research with the Satellite Meteorology and Climatology Center, NOAA/NESDIS, College Park, MD, USA, a Senior Scientist of the Joint Center for Satellite Data Assimilation,, College Park, MD, USA, and a JPSS Sensor Science Chair. He has authored over 150 papers in American journals (e.g., AMS, AGU, and IEEE) and other international journals.

Dr. Weng received a number of awards including the First Winner of the 2000 NOAA David Johnson Award for his outstanding contributions to satellite microwave remote sensing fields and the utilization of satellite data in the NWP models, the U.S. Department of Commerce Gold Medal Award in 2005 for his achievement in satellite data assimilation, the NOAA Bronze Medal for leading successful NOAA-18 instrument calibration, and the NOAA Administrator's Award for developing new and powerful radiative transfer models to assimilate advanced satellite data.

Ninghai Sun received the Ph.D. degree from the University of Maryland, College Park, MD, USA, in 2010.

He is currently leading the development of NESDIS/STAR ICVS system and is a Technique Lead of the Advanced Technology Microwave Sounder Instrument SDR Team.

Kent Anderson received the B.S. and M.S. degrees in electrical engineering from the Rose Hulman Institute of Technology, Terre Haute, IN, USA, in 1971 and 1972, respectively.

He has 30-year experience in systems engineering for spaceborne remote sensing systems. For the last 15 years, he has been the Lead Systems Engineer for Civil Space Programs with Northrop Grumman Electronic Systems, Azusa, CA, USA, focused primarily on millimeter-wave radiometry, particularly for the Advanced Technology Microwave Sounder Program. His research interests include requirements management, initial design trade studies, performance analyses, and analyses of test data.

Quanhua Liu received the B.S. degree from the Nanjing University of Information Science and Technology, Nanjing, China, in 1982, the master's degree in physics from the Chinese Academy of Sciences, Beijing, China, in 1984, and the Ph.D. degree in meteorology and remote sensing from the University of Kiel, Kiel, Germany, in 1991.

He is currently a Physical Scientist with the Center for Satellite Application and Research, National Oceanic and Atmospheric Administration, National Environmental Satellite, Data, and Information Service, College Park, MD, USA, where he is involved in Advanced Technology Microwave Sounder sensor data calibration and microwave integrated retrieval system. His research interests include the development of the community radiative transfer model that operationally supports satellite radiance assimilation for weather forecasting and the Joint Polar Satellite System/Suomi National Polar-orbiting Partnership and GOES-R missions for instrument calibration, validation, long-term trend monitoring, and satellite retrieved products.

Edward J. Kim received the S.B. and S.M. degrees in electronic engineering from MIT, Cambridge, MA, USA, in 1986 and 1989, respectively, and the joint Ph.D. degree in electrical engineering and computer science from the Department of Atmospheric, Oceanic, and Space Sciences, University of Michigan, Ann Arbor, MI, USA.

His research interests include developing and applying remote sensing techniques to monitor and understand the earth system—particularly snow, field measurement and modeling of snow, snow radiative transfer theory, radiance data assimilation, microwave remote sensing instruments, microwave radiometer calibration and intercalibration, and radio frequency interference detection and mitigation.